

Numerical simulations of two-phase flows in high-permeability porous media: Effect of the permeability on the drag force between fluids and fluid-solid phases

Maxime Cochennec,^{1,2} Hossein Davarzani,^{1,*} Stéfan Colombano,¹ Ioannis Ignatiadis,¹
Yohan Davit,³ and Michel Quintard³

¹*French Geological Survey (BRGM),
45060 Orléans,
France*

²*Agence de l'environnement et de la maîtrise de l'énergie (ADEME),
Angers,
France*

³*Institut de Mécanique des Fluides de Toulouse (IMFT),
Université de Toulouse,
CNRS,
France*

Abstract

The macroscopic description of two-phase flows in porous media requires accurate modelling of the drag forces between the two fluids and the solid phase. In standard porous media, where capillarity is often dominant, the fluid-solid interactions are well-known and the fluid-fluid drag force is treated in a similar way as the drag between fluids and solid in the momentum transport equation. Two-phase flows in highly permeable porous media, however, are often characterized by a larger area of the interface between the two fluids and the development of thin films. In such cases, the fluid-fluid drag is not necessarily negligible and may play an important role in the momentum transport equations. Here, we use computational methods to study two-phase flows in a microfluidic device made of an array of cylinders squeezed between two plates in a Hele-Shaw flow cell. The distinguishing feature of this work is to solve an amalgam Stokes-Darcy equations. Tangential stresses are handled by the Stokesian part whereas the confinement in the out-of-plane direction is controlled by the Darcean term. Thus, we explore different ranges of permeability by changing the gap h between the plates whereas the geometry in the cell plane is unmodified. The key question addressed in this work is the importance of the fluid-fluid drag forces in the overall pressure loss during cocurrent two-phase flows and how the flow confinement and the capillary number affect the repartition of the drag forces.

* Corresponding author:

h.davarzani@brgm.fr

I. INTRODUCTION

An accurate description of two-phase flows in high-permeability porous media is of major importance in several practical applications. This includes soil remediation in sandy or gravelly soils (Fetter et al., 2017), nuclear safety (Clavier et al., 2017), or catalytic fixed bed reactors (de Santos et al., 1991). However, most of the literature on two-phase flows in porous media is focused on low-permeability porous media. For low-permeability porous media in the limit of creeping flows, surface tension forces often dominate the flow; thus the capillary, Bond, and Weber numbers are low. In that case, the fluid repartition is well described as two independent flow paths for each phase (Blunt, 2017; Dullien, 2012). The two fluids are segregated, the non-wetting fluid flows into the larger pores, whereas the wetting fluid occupies the smaller pores. One of the consequences is that the area of the fluid-fluid interface is small (Fig. 1 (a)) and there is little drag between the fluid phases. In contrast, for high-permeability porous media, the flow is the result of a complex interaction between capillary, gravity, viscous, and inertial forces (Davit and Quintard, 2018). Capillary effects may no longer dominate and the capillary, Bond, and Weber numbers may be large. The distribution of fluids in the pore space can be schematically decomposed in two modes, even though the reality is often a lot more complex. Either the non-wetting fluid is continuous and flows in the center of the pores surrounded by the wetting fluid flowing as a thin film in contact with the solid (Fig. 1 (b)), or the non-wetting fluid is discontinuous and flows in the center of the pores in the form of droplets or ganglia (Fig. 1 (c)). In both cases, the surface area between the fluids is large and the drag forces between the fluids are not negligible compared with the solid-fluids drag forces. This is in strong contrast with capillarity-dominated flow and it is of major importance since, as discussed in the following, modelling of the drag forces is the basis of any attempt to establish continuous relationships on a macroscopic scale starting from the pore scale.

Models used to describe two-phase flows in porous media are often based on a direct extension of Darcy's equations for one-phase flow (Muskat, 1938; Wyckoff and Botset, 1936). This generalization depends on the introduction of relative permeabilities that essentially account for the division of the available void space between the fluids; thus each fluid phase acts as a supplementary solid regarding the other one and no interaction between the phases is taken into account (Blunt, 2017; Dullien, 2012). As a consequence, it is commonly assumed that the relative permeability only depends on the saturation (Brooks and Corey, 1964; Van Genuchten,

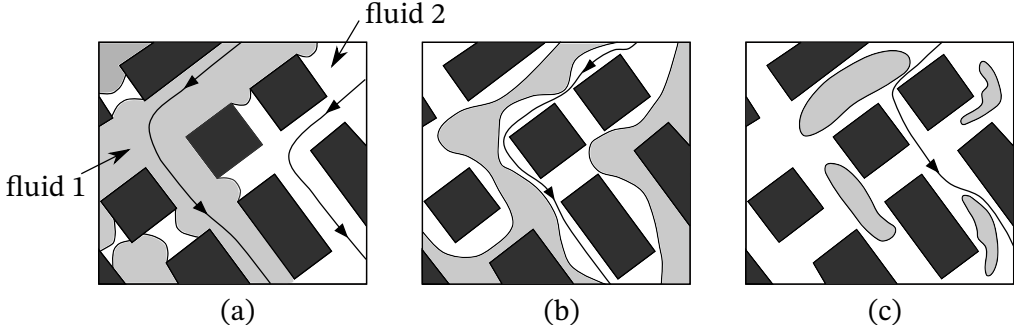


Figure 1 Schematics of possible distributions of fluids in a 2D porous network with solid phase in black, the non-wetting fluid (fluid 1) in light grey, and the wetting fluid (fluid 2) in white, (a) the two fluids are flowing in different channels separated by numerous meniscus and the fluid-fluid interface extent is small, (b) the wetting and non-wetting fluids are flowing together in most of the pores as two continuous streams and (c) both fluids are flowing together in most of the pores and the non-wetting phase is discontinuous. - Adapted from ([Dullien, 2012](#))

[1980](#)) and we know that this is not always accurate as relative permeabilities may also depend on the capillary number ([Li et al., 2005](#)), the flow regime ([Avraam and Payatakes, 1995](#)) or the viscosity ratio ([Ehrlich, 1993; Yiotis et al., 2007; Yuster et al., 1951](#)). Since the early 1980s, numerous works have aimed at improving the generalized Darcy equations on a sound physical basis. Using upscaling techniques, several authors proposed additional coupling terms that correspond to stresses at the fluid-fluid interface and yield coupling permeability tensors ([Auriault and Sanchez-Palencia, 1986; Lasseux et al., 1996; Marle, 1982; Whitaker, 1986](#)). The importance of these coupling terms in the overall flow process is not clear ([Ayub and Bentsen, 1999](#)). These additional terms can be calculated analytically in a two-phase annular cocurrent flow in a cylindrical capillary tube, and are of the same order as the dominant relative permeabilities ([Bacri et al., 1990](#)). However, other studies considered configurations for which the surface between fluids was smaller and concluded that coupling terms should not be as important ([Rakotomalala et al., 1995; Scott et al., 1953](#)). [Zarcone and Lenormand \(1994\)](#), [Dullien and Dong \(1996\)](#) and [Ramakrishnan and Goode \(2015\)](#) directly measured the coupling permeability terms in natural media by performing steady-state cocurrent two-phase flows. [Rose \(1988\)](#) proposed to indirectly measure the coupling relative permeability terms by performing two different types of experiments. This technique was also used for both cocurrent and countercurrent experiments ([Bentsen and Manai, 1993; Bourbiaux et al., 1990](#)). Each of these authors, except Zarcone and Lenormand, found that the coupling relative permeabilities are

significant. Recently, [Clavier et al. \(2017\)](#) performed experiments of inertial two-phase flows in coarse non-consolidated porous media and proposed constitutive models. However, results suffer from a major shortcoming. Indeed, it is impossible to know which type of flow regime dominates at the pore scale and thus the exact link between the physics at the pore-scale and the macroscale model.

Micromodels can be used to better understand two-phase flows in porous media ([Karadimitriou and Hassanzadeh, 2012](#)), e.g. transitions between the flow regimes or the onset and development of displacement instabilities ([Lenormand et al., 1988; Zhang et al., 2011](#)). Therefore, micromodels allow overcoming the major issue we have just risen. Such apparatus were employed to measure the relative coupling permeabilities for different flow regimes ([Avraam and Payatakes, 1995](#)) or study the impact of the fluid-fluid drag on the flow characteristics ([Heshmati and Piri, 2018; Roman et al., 2019](#)). [Rothman \(1990\)](#) used numerical simulations in a 2D micromodel geometry and found that coupling permeabilities are comparable in magnitude with the case of the annular flow in a capillary tube. Fig. 2 shows Rothman's results along with some of the previously mentioned results on relative coupling permeabilities. Hele-Shaw cells are one of the simplest example of micromodels as they consist of two parallel plates which form a thin gap in which the fluids can flow. A large body of work has focused either on the displacement of a bubbles and drops in Hele-Shaw cells ([Kopf-Sill and Homsy, 1988; Maruvada and Park, 1996; Maxworthy, 1986](#)) on the stability of the fluid front during the displacement of a fluid by another less viscous fluid ([Bensimon, 1986; Cueto-Felgueroso and Juanes, 2014; Jackson et al., 2017; Meiburg and Homsy, 1988; Saffman and Taylor, 1958](#)). The governing flow equations in Hele-Shaw cells are analogous to Darcy's equation, therefore several studies used Hele-Shaw cells to gain insight about two-phase flow in porous media ([Homsy, 1987; Liu et al., 2019; Stokes et al., 1986](#)). Here, we study the influence of micro-model's absolute permeability on the fluid-fluid drag and solid-fluids drag for different capillary numbers. The distinguishing feature of the article is to solve an amalgam Stokes-Darcy equations for two-phase flows in a Hele-Shaw cell with wedge to study the effect of the varying absolute permeability on the drag forces without having to change the in-plane geometry.

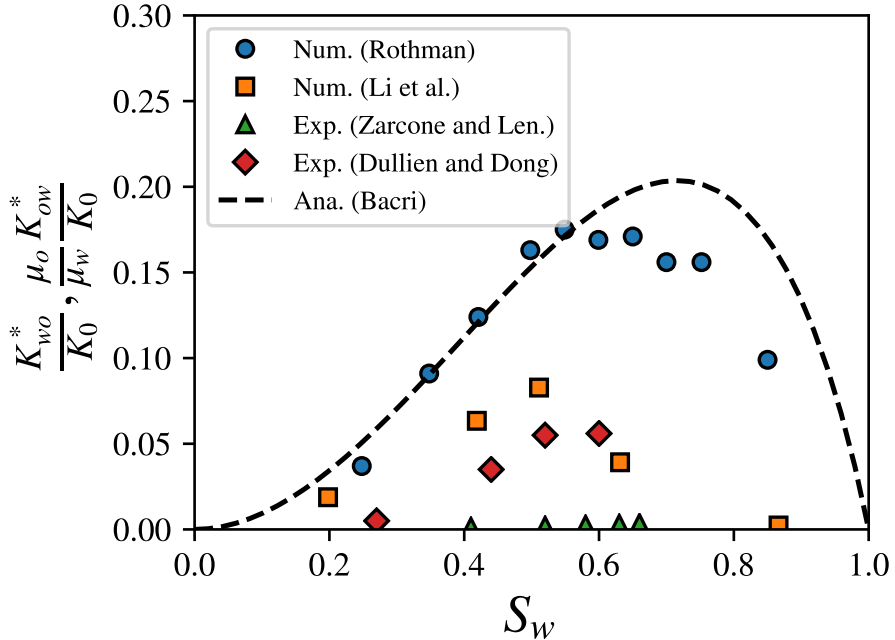


Figure 2 Normalized coupling relative permeabilities K_{ij}^* as a function of the wetting-fluid saturation S_w from experimental work (Dullien and Dong, 1996; Zarcone and Lenormand, 1994), numerical simulations (Li et al., 2005; Rothman, 1990) and analytical solution for a steady-state annular two-phase flow in a circular capillary tube (dashed line) (Bacri et al., 1990). The capillary theoretical case provides an upper limit in terms of permeability and extent of the interfacial surface area between the fluids.

II. PORE-SCALE, DEPTH-AVERAGED AND VOLUME-AVERAGED FLOW EQUATIONS

In this section, we present the derivation of the averaged flow equations for two-phases flows in a Hele-Shaw cell, starting from the three-dimensional Stokes equations. Then, we average the momentum equations spatially to derive the unclosed form of the macroscopic momentum transport equations. The system under consideration is depicted in Fig. 3 which represents a quasi-planar cocurrent two-phase flow between two parallel plates with a wedge of circular cross-section as a solid obstacle. The transverse dimension of the cell is noted L and h is the length of the gap between the plates.

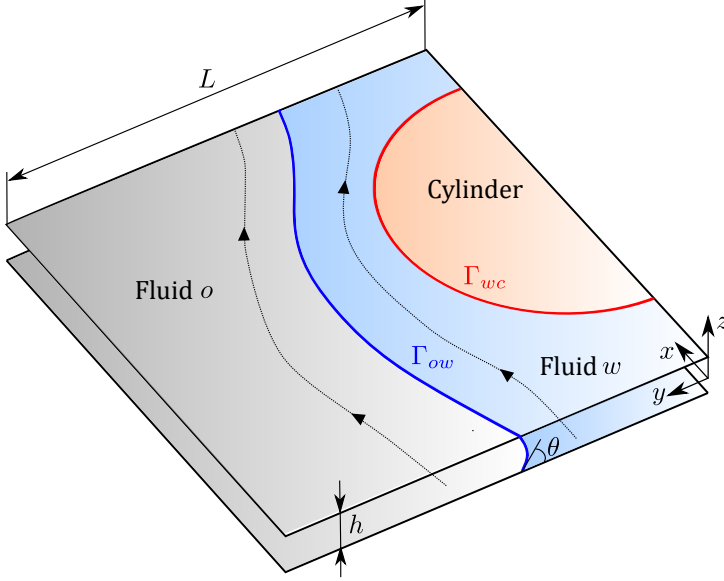


Figure 3 Schematic view of a cocurrent two-phase flow in a Hele-Shaw cell parallel to the $x - y$ plane with a wedge of circular cross-section as a solid obstacle. The transverse dimension of the cell is noted L and h stands for the gap between the plates. The boundary between the wetting-fluid w and the cylinder (in red) is noted Γ_{wc} and the boundary between the two fluids (in blue) is noted Γ_{ow} . No dynamic films along the plates are considered here and θ stands for the non-zero contact angle between the two fluids and the plates.

A. Pore-scale flow equations

Three-dimensional continuity and Stokes equations for a Newtonian fluid in the absence of external forcing read, respectively,

$$\nabla^* \cdot \mathbf{u} = 0, \quad -\nabla^* p + \mu \nabla^{*2} \mathbf{u} = 0, \quad (1)$$

where the superscript * indicates that the derivative operators are three-dimensional.

B. Depth-averaged flow equations

The starting point is to consider an apparatus such as depicted in Fig. 3 for which h is very small compared to the transverse length of the cell. It follows that the z -component of the velocity can be neglected (Guyon et al., 1994) and the velocity field

$$\mathbf{u} = (u(x, y, z), v(x, y, z), 0)^T = f(z)\bar{\mathbf{u}}(x, y), \quad (2)$$

where we introduce the depth-averaged velocity defined as $\bar{\mathbf{u}} \equiv \frac{1}{h} \int_{-h/2}^{h/2} \mathbf{u} dz$. The in-plane version of Eq. 1 then read

$$\nabla \cdot \bar{\mathbf{u}} = 0, \quad -\nabla p + \mu \left(\nabla^2 \bar{\mathbf{u}} + \bar{\mathbf{u}} \frac{\partial^2 f(z)}{\partial z^2} \right) = 0. \quad (3)$$

From the condition $\int_{-h/2}^{h/2} f(z) dz = h$, arising from the definition of the depth-averaged velocity, along with the no-slip boundary condition at $z \pm h/2$, we find that $f(z) = \frac{3}{2}(1 - 4\frac{z^2}{h^2})$. Then,

$$\nabla \cdot \bar{\mathbf{u}} = 0, \quad \mu (\nabla^2 \bar{\mathbf{u}} - k^2 \bar{\mathbf{u}}) = \nabla p, \quad (4)$$

are the continuity and momentum transport equations for the depth-averaged flow of one fluid and $k = \sqrt{12}/h$. It has been shown that the velocity profile for a flow in a rectangular channel with Eq. 4 lead to a reasonable approximation, up to aspect ratios $h/L = 1$, of the result obtained from the three-dimensional Stokes equations ([Nagel and Gallaire, 2015](#)). In the case of two-phase flows, these equations have to be written for each fluid and boundary conditions at the fluid-fluid interfaces are required. Continuity of the depth-averaged velocities across the interface and a jump of interface normal stress are sufficient if the surface tension is constant along the interface ([Park and Homsy, 1984](#)). These conditions are expressed

$$\bar{\mathbf{u}}_o - \bar{\mathbf{u}}_w = 0 \text{ at } \Gamma_{ow}, \quad (5)$$

$$(\bar{\sigma}_w - \bar{\sigma}_o) \cdot \mathbf{n}_{ow} = \gamma \left(\frac{\pi}{4} \kappa_{\parallel} + \frac{2}{h} \cos \theta \right) \mathbf{n}_{ow} \text{ at } \Gamma_{ow}, \quad (6)$$

where $\bar{\sigma}_i$ is the in-plane stress tensor of fluid i , \mathbf{n}_{ow} is the in-plane normal vector at the fluid interface pointing toward the fluid w , γ is the surface tension, κ_{\parallel} is the in-plane interface curvature and θ denotes the contact angle between the fluid interface and the plates (Fig. 3). The meniscus in the z -direction is approximated as a half-circle of radius $h/2$ and the $\pi/4$ correction for the in-plane curvature was derived by [Park and Homsy \(1984\)](#). In Eq. 6, we neglected the additional terms that pertain to the formation of the dynamic film ([Park and Homsy, 1984](#)) which scaled non-linearly with the capillary number. We rather considered a non-zero contact angle, and consequently, the absence of such thin films.

C. Volume-averaged flow equations

Here, we proceed to the spatial averaging of the in-plane momentum transport equations. We recall that all the flow variables and differential operators have components only in the transverse direction. According to the volume averaging framework (Whitaker, 2013) and acknowledging that Eq. 4 are two-dimensional, the traditional averaging theorem for the depth-averaged quantity $\bar{\omega}_i$ associated with the fluid i reads

$$\langle \nabla \bar{\omega}_i \rangle = \nabla \langle \bar{\omega}_i \rangle + \frac{1}{S} \int_{\Gamma_{ic}} \mathbf{n}_{ic} \bar{\omega}_i \, d\Gamma + \frac{1}{S} \int_{\Gamma_{ij}} \mathbf{n}_{ij} \bar{\omega}_i \, d\Gamma, \quad (7)$$

where,

$$\langle \bar{\omega}_i \rangle = \frac{1}{S} \int_{S_i} \bar{\omega}_i \, dS, \quad (8)$$

is the superficial surface average and S is the surface of a representative elementary cell. Applying the superficial surface average of Eq. 4 along with the averaging theorem and using traditional length-scale arguments (Whitaker, 2013) we obtain

$$\nabla \cdot \langle \bar{\mathbf{u}}_i \rangle = 0, \quad i, j = o, w, i \neq j, \quad (9a)$$

$$\begin{aligned} & \frac{1}{S} \int_{\Gamma_{ic}} \mathbf{n}_{ic} \cdot \left(-p_i \mathbf{I} + \mu_i (\nabla \bar{\mathbf{u}}_i + (\nabla \bar{\mathbf{u}}_i)^T) \right) \, d\Gamma + \\ & + \frac{1}{S} \int_{\Gamma_{ij}} \mathbf{n}_{ij} \cdot \left(-p_i \mathbf{I} + \mu_i (\nabla \bar{\mathbf{u}}_i + (\nabla \bar{\mathbf{u}}_i)^T) \right) \, d\Gamma - \\ & - \mu_i k^2 \langle \bar{\mathbf{u}}_i \rangle = \varepsilon_i \nabla \langle p_i \rangle^i + \langle p_i \rangle^i \nabla \varepsilon_i, \quad i, j = o, w, i \neq j, \end{aligned} \quad (9b)$$

where \mathbf{I} is the 2×2 identity matrix and $\langle p_i \rangle^i$ ($\langle p_i \rangle^i = \langle p_i \rangle / \varepsilon_i$) is the intrinsic surface average pressure of fluid i , with ε_i the volume fraction of fluid i . The first integral is the drag force exerted upon the cylinders boundary by fluid i and the second integral pertains for the drag force exerted upon fluid j by fluid i . Here, we consider that the contour of the fluid-fluid interface in the $x - y$ plane can be identically translated along the z -direction, which is an approximation since the meniscus is a half-circle for small h/L ratio. However, as shown in the A, using three-dimensional flow simulations in microchannels, these approximations remain reasonable.

Drag of...	Fluid o	Fluid w	
upon...			
Plates	$-\mu_o \langle \bar{\mathbf{u}}_o \rangle \frac{12}{h^2}$	$-\mu_w \langle \bar{\mathbf{u}}_w \rangle \frac{12}{h^2}$	$ \Sigma = d_s$
Wedge	-	\mathbf{d}_{wc}	
Fluid o	-	\mathbf{d}_{wo}	$ \Sigma = d_f$
Fluid w	\mathbf{d}_{ow}	-	

Table I Summary of each drag force terms involved in the averaged momentum transport equation for two-phase flow in a Hele-Shaw cell.

If the variation of the saturation in space is negligible and acknowledging that, as illustrated in Fig. 3, only the wetting fluid w is in contact with the wedge, a more compact form of Eq. 9b reads

$$0 = -\varepsilon_w \nabla \langle p_w \rangle^w - \mu_w k^2 \langle \bar{\mathbf{u}}_w \rangle + \mathbf{d}_{wc} + \mathbf{d}_{wo}, \quad (10a)$$

$$0 = -\varepsilon_o \nabla \langle p_o \rangle^o - \mu_o k^2 \langle \bar{\mathbf{u}}_o \rangle + \mathbf{d}_{ow}, \quad (10b)$$

where, \mathbf{d}_{ij} ($\mathbf{d}_{ij} = \frac{1}{S} \int_{\Gamma_{ij}} \sigma_i \cdot \mathbf{n}_{ij} d\Gamma$) denotes the drag forces per unit surface area exerted upon phase j by phase i and which must be computed or modeled to obtain closed macroscopic equations. In the following, we are working on the direct calculation of each drag force terms summarized in Tab. I.

III. DIRECT NUMERICAL SIMULATIONS

In this section, we introduce the standard Level Set method to capture the moving free interface between the fluids, along with the flow equations, both solved with a Finite Element solver.

A. Equations

The Level Set method is an Eulerian method that easily handles the topological phases changes, in contrast with Lagrangian methods. Here, the fluid phases are identified with a phase color function that goes smoothly from 0 to 1 across the fluid interface with the manifold defined as the iso-level $\phi = 0.5$. Transport of the level set function ϕ is governed by

$$\frac{\partial \phi}{\partial t} + \nabla \cdot (\bar{\mathbf{u}}\phi) = \tau \nabla \cdot \left(\psi \nabla \phi - \phi(1-\phi) \frac{\nabla \phi}{|\nabla \phi|} \right), \quad (11)$$

where $\bar{\mathbf{u}}$ is the depth-averaged velocity field and τ and ψ are two numerical parameters that control the diffuse interface thickness and the amount of initialization of ϕ function, respectively (Olsson et al., 2007). We investigated the accuracy of the implicit definition of the interface as well as the effect of the value of the initialization parameter on the interface position in B by comparing to a boundary element method (Nagel and Gallaire, 2015).

The governing flow equations read

$$0 = \nabla \cdot \bar{\mathbf{u}} \quad (12a)$$

$$0 = -\nabla p + \mu(\phi) \left(\nabla^2 \bar{\mathbf{u}} - \frac{12}{h^2} \bar{\mathbf{u}} \right) + \gamma \left(\frac{\pi}{4} \nabla \cdot \left(\frac{\nabla \phi}{|\nabla \phi|} \right) - \frac{2}{h} \right) \delta(\phi) \mathbf{n}, \quad (12b)$$

where δ is the Dirac delta function localized on the interface and \mathbf{n} denotes the unit normal to the interface, respectively defined as,

$$\delta(\phi) = 6 |\nabla \phi| |\phi(1+\phi)|, \quad \text{and} \quad \mathbf{n} = \frac{\nabla \phi}{|\nabla \phi|}. \quad (13)$$

We introduce the following reference and dimensionless quantities,

$$\bar{\mathbf{u}} = \bar{\mathbf{u}}' \times U_r, \quad p = p' \times \frac{\mu_r U_r}{L}, \quad \mathbf{x} = \mathbf{x}' \times L, \quad (14)$$

and the dimensionless continuity and momentum transport equations are

$$0 = \nabla' \cdot \bar{\mathbf{u}}' \quad (15a)$$

$$0 = -\nabla' p' + \frac{\mu(\phi)}{\mu_r} \left(\nabla'^2 \bar{\mathbf{u}}' - \frac{12}{(h/L)^2} \bar{\mathbf{u}}' \right) + \frac{\gamma}{\mu_r U_r} \left(\frac{\pi}{4} \nabla' \cdot \left(\frac{\nabla' \phi}{|\nabla' \phi|} \right) - \frac{2}{h/L} \right) \delta'(\phi) \mathbf{n}, \quad (15b)$$

with $\delta'(\phi) = 6 |\nabla' \phi| |\phi(1+\phi)|$. We therefore have three dimensionless numbers: the viscosity ratio $M(\phi) = \frac{\mu(\phi)}{\mu_r}$, the capillary number $Ca^{-1} = \frac{\gamma}{\mu_r U_r}$ and the aspect ratio $h^* = h/L$.

B. Geometry, boundary conditions and simulation parameters

Our macroscopic model is a Hele-Shaw cell with wedges of cylindrical cross-section. This system is subdivided into seven unit-cell (UC) subdomains encompassing one wedge, as depicted in Fig. 4. Taking advantage of the symmetry, we studied only the upper half of a row. Each fluid flows from left to right (x -direction) and the inlet boundary conditions for both fluids are a constant normal inlet velocity u_i . The outlet boundary condition for the flow is

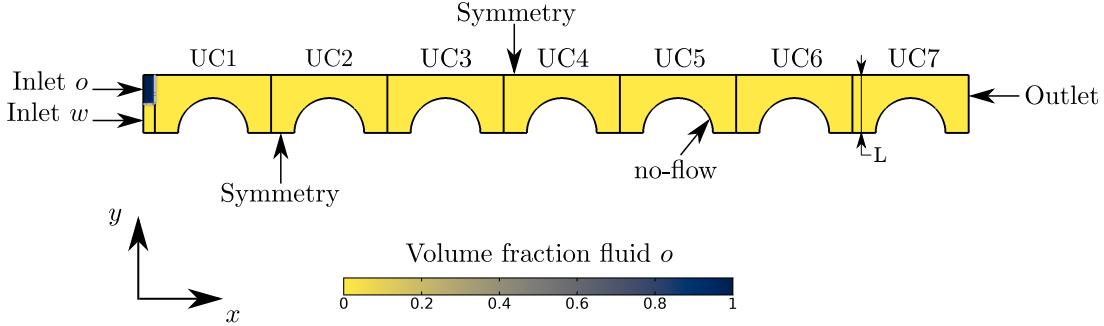


Figure 4 Schematics of the geometry and initial condition. We consider the superior half of an array of five cylindrical wedges inside five cuboids where both fluids are injected from left to right. Initially, the model is saturated with wetting fluid (red), and the width L of one Unit Cell (UC) is 5×10^{-4} m. Symmetry boundary conditions are used on both length sides and the no-flow boundary condition is imposed at the wedge boundary.

a reference pressure. The boundary conditions used are summarized in Tab. II. We choose the total inlet velocity as the reference velocity; thus the dimensionless inlet velocities can be expressed as a fractional flow f_f ,

$$f_f = \frac{u_w}{U_t}, \quad u_o = 1 - f_f, \quad \text{with} \quad U_t = u_w + u_o. \quad (16)$$

The non-wetting viscosity is taken as the reference viscosity and the respective value of each dimensionless parameters is in Tab. II. The initialization parameter value is equal to the maximum inlet velocity value, which yields maximum accuracy (Appendix B). As a reference, we conducted numerical simulations of one-phase flows and found that the range of gap corresponds to a range absolute permeabilities between 1.5×10^4 and 40 darcy.

C. Mesh sensitivity analysis

Here, we study the mesh convergence of various drag forces. The dimensionless numbers for this study are $Ca = 1.25 \times 10^{-1}$, $h^* = 1/4$, $f_f = 0.25$ and $M = 1$. In Fig. 5 (a) the results are normalized with respect to the finer mesh result and are given as a function of the total number of degree of freedom in the whole model. The fluid-fluid interface position for three different mesh densities is given in Fig. 5 (b). We obtain these results in the fourth unit-cell (UC4) at steady-state. The drag terms are not very sensitive to the mesh density and the

Table II Boundary conditions for flow variables and the Level Set function (left) and simulation parameters (right).

Boundary	u	p	ϕ
Outlet	-	0	$\mathbf{n} \cdot \nabla \phi = 0$
Inlet o	u_o	-	0
Inlet w	u_w	-	1

Parameters	Value
$Ca = \frac{U_t \mu_o}{\gamma}$	from 1.25×10^{-1} to 5×10^{-3}
$M_w = \frac{\mu_w}{\mu_o}$	1
$f_f = \frac{u_w}{U_t}$	1/4
$h^* = h/L$	from 5 to 1/20

interface between the fluids is correct even for a coarse mesh and converges quickly. In the following simulations, we use a mesh that corresponds to 3.7×10^5 degree of freedoms

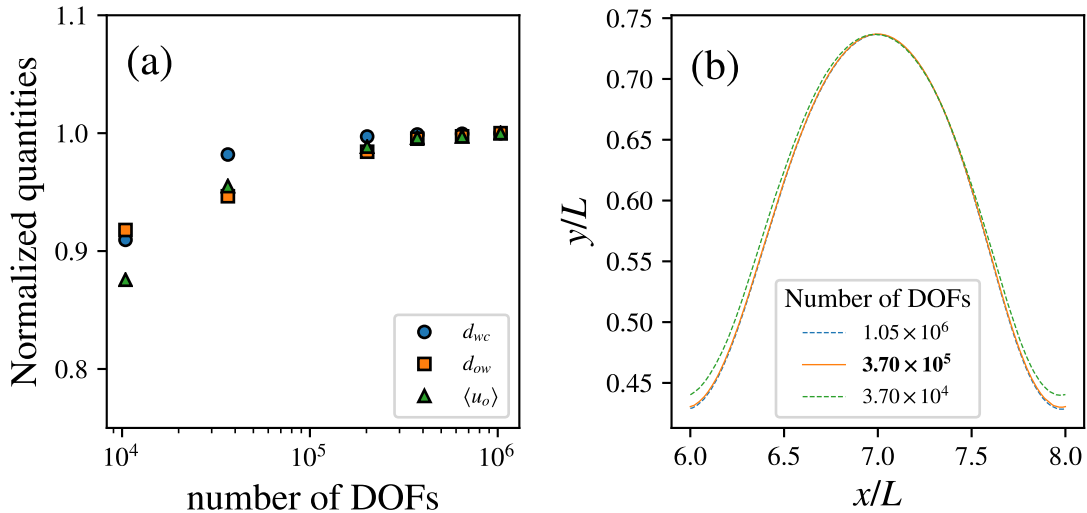


Figure 5 Mesh convergence study of (a) drag force exerted upon the wedge (blue), drag force exerted upon the fluid-fluid boundary (orange) and intrinsic average velocity of fluid o (green). All the results are normalized with respect to the result obtained with the finer mesh, at steady-state and in UC4. (b) Fluid-fluid interface position in UC4 at steady-state for different number of degree of freedoms in the whole geometry. Flow parameters are $Ca = 1.25 \times 10^{-1}$, $h^* = 1/4$, $f_f = 0.25$ and $M = 1$. In the following we use a mesh that corresponds to 3.7×10^5 degree of freedoms.

IV. RESULTS

We now present the study of the co-current two-phase flows in the aforementioned micromodel. The results section is organized as follows. We start in §IV.A with a description of the flow regime observed under the selected flow parameters. The flow regime is fundamental as it drives the extent of the interfacial surface area between the fluids and therefore the amount of fluid-fluid drag. The saturation and the fluid-fluid interface is also presented as a function of the gap thickness and capillary numbers. In §IV.B we discuss the effect of the flow confinement, i.e. the permeability, on the velocity and pressure fields. Then we calculate in §IV.C each drag terms in Eq. 10. Two limit regimes are identified in term of gap thickness.

A. Flow regimes and fluids saturation

We observe that the two fluids remain continuous at all times and for the entire range of tested capillary numbers and gap thickness. The interface between the fluids becomes stationary and steady-state is reached for every capillary number and values of gap thickness. Fig. 6 shows the initial, intermediate, and final configurations of the fluid repartition for $Ca = 1.25 \times 10^{-1}$ and $h^* = 1/8$. The fluid-fluid interface is periodic on the five central unit cells at steady-state whereas the interface is slightly deformed at the inlet and outlet cells, under the influence of boundary conditions.

The penetration of the non-wetting fluid shown in Fig. 6 does not result from an instable displacement, i.e. viscous fingering, since both fluids have the same viscosity. Here, non-wetting phase break-up could have occurred either by snap-off phenomenon or because of the shear exerted by the wetting fluid. However, the pore throat is large and the fractional flow is low, which favours the continuity of the non-wetting fluid phase. The flow-regime observed is therefore a film-flow regime within the limit of the parameters chosen for this study.

Fig. 7 shows the wetting fluid saturation as a function of the dimensionless gap between the plates and for different capillary numbers. Wetting fluid saturation at steady-state decreases, in average, from 0.6 to 0.4 as the aperture between the plates decreases from 5 to 1/20. The results for the larger gap are identical to the purely 2d results. The saturation fields insets in Fig. 7 indicate that the fluid-fluid interfaces are very similar for the thinnest gap whereas they

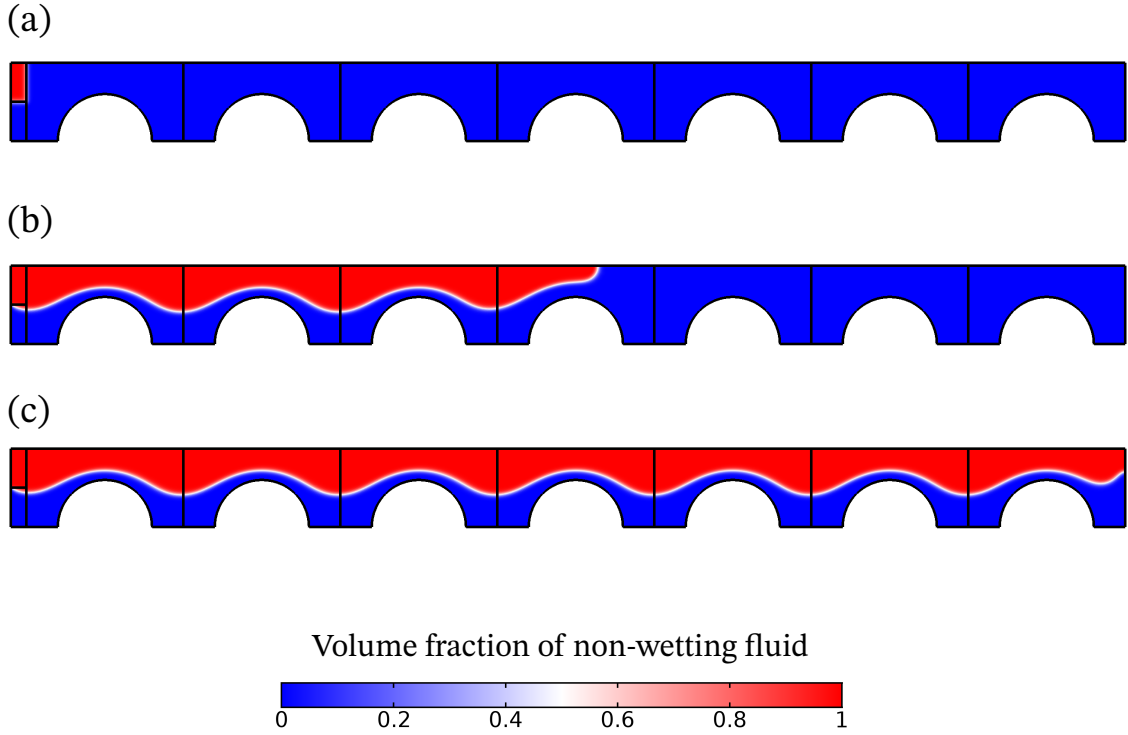


Figure 6 Fluids repartition along the superior half-row at (a) the initial time, (b) for an intermediate time and (c) final time (steady-state reached) for $Ca = 1.25 \times 10^{-1}$, $f_f = 0.25$, $M = 1$ and $h^* = 1/8$. At steady-state the fluid-fluid interface taken on the central unit cells is periodic whereas it is slightly deformed in the first and last UC under the influence of the boundary conditions.

largely differ for thinner gaps. This last point explains the different saturation we observed. Indeed, for low capillary number the interface is flatter than for high capillary numbers, as shown in Fig. 8. Two configurations are possible, either the capillary number is high and the fluid-fluid interface is mostly translated toward the pore throat as the gap increases, or the capillary number is low enough that the fluid-fluid interface is deformed (flattened) and also pushed towards the pore throat for an increasing gap thickness. These different fluid configurations might involve substantial differences in the velocity and pressure fields, for example by forming narrow channel with high local velocity, which ultimately may impact the amount of drag.

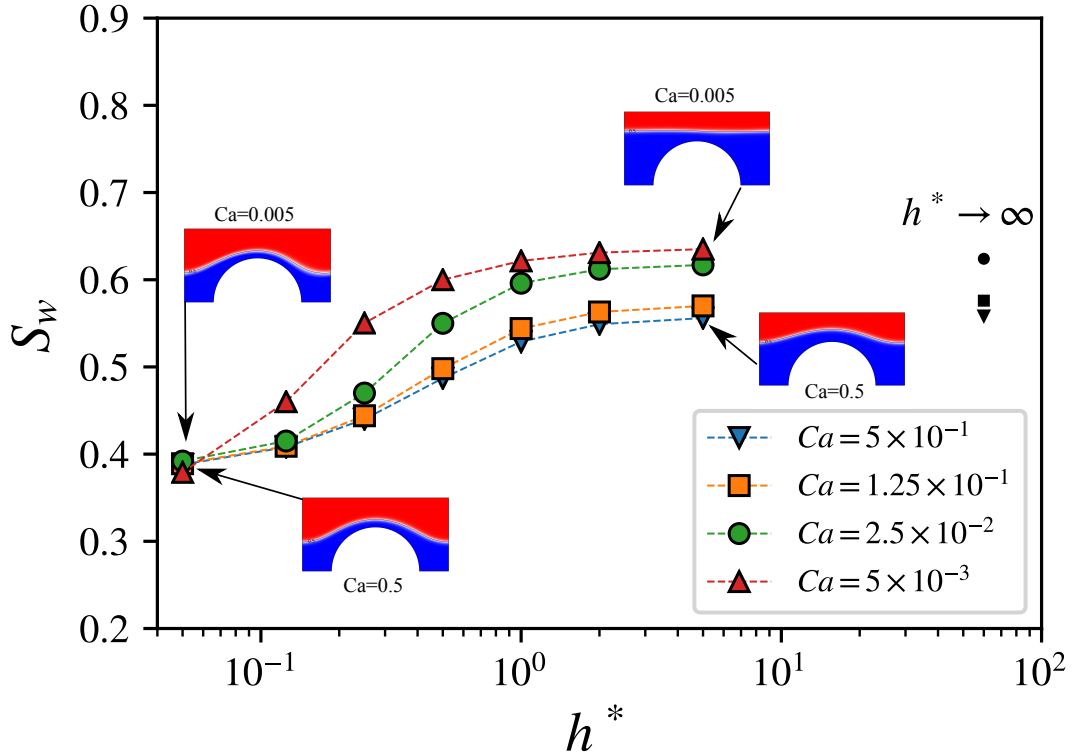


Figure 7 Fluid saturation at steady-state in UC4 as a function of the dimensionless gap and for different capillary numbers. Fields of the level-set function at steady-state in UC4 are given for the selected value of the dimensionless gap and $Ca = 1.25 \times 10^{-1}$ and $Ca = 5 \times 10^{-3}$. As the gap increases the interface flattens and the wetting fluid saturation increases. A decrease in the capillary number acts in the same way, albeit less strongly. The 2D limit case is given with plain black markers.

B. Pressure and velocity fields

Fig. 9 shows the pressure field for selected values of capillary number and gap thickness. The main point here is that the pressure jump across the fluid-fluid interface is very difficult to distinguish for the higher capillary number $Ca = 5 \times 10^{-1}$, and especially for the thinnest gap, for which the pressure is uniform across the interface. That was to be expected since the main pressure contribution to the pressure jump arises from the out-of-plane curvature and thus scales as h^{-1} , whereas the pressure gradient across the cell scales as h^{-2} for very thin gap, for which the Darcian terms are expected to be dominant. In contrast, the pressure jump is clearly visible for the lower capillary number $Ca = 2.5 \times 10^{-2}$. In this last case we see that

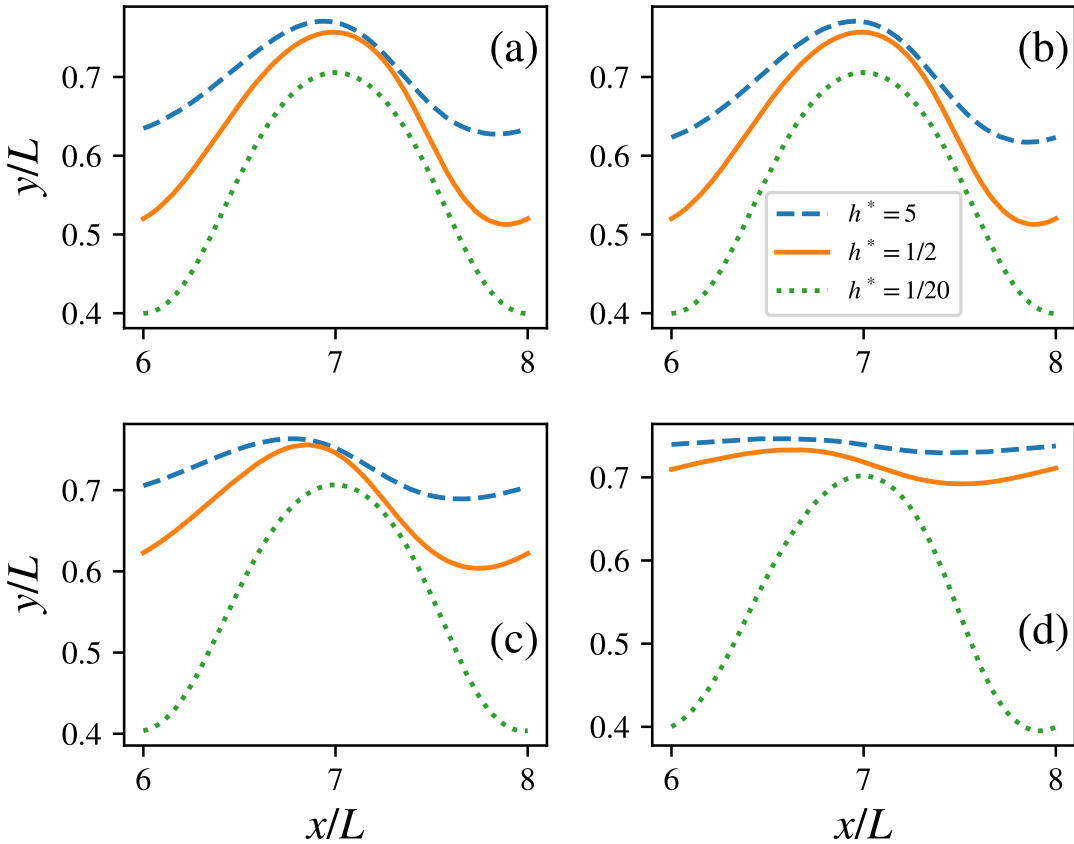


Figure 8 Comparison of the fluid-fluid interface at steady-state in UC4 for different dimensionless gaps between the plates. The interfaces are almost symmetric for (a) interface $Ca = 5 \times 10^{-1}$ and (b) $Ca = 1.25 \times 10^{-1}$. The interfaces are flatten for larger gaps for (c) $Ca = 2.5 \times 10^{-2}$ and (d) $Ca = 5 \times 10^{-3}$ (results in UC4 after steady-state was reached for $f_f = 0.25$ and $M = 1$).

the pressure is higher in the non-wetting fluid, which is in agreement with the out-of-plane meniscus. Fig. 10 shows the velocity field normalized with respect to the reference velocity for the same selected parameters than for the pressure fields. We plot also the corresponding streamlines and the position of the fluid-fluid interface and we distinguish three cases. For the thinnest gap ($h^* = 1/20$), the velocity fields are identical regardless of the capillary number. In this case the maximum velocity is reached in the center of the pore throat and between the fluid-fluid interface and the wedge boundary. In contrast the velocity field depends on the capillary number for the thickest gap. Either the capillary number is high and the maximum velocity is reached precisely in the center of the pore throat or the capillary number is lower and the maximum velocity is slightly offset from the centre to directly overhang the fluid in-

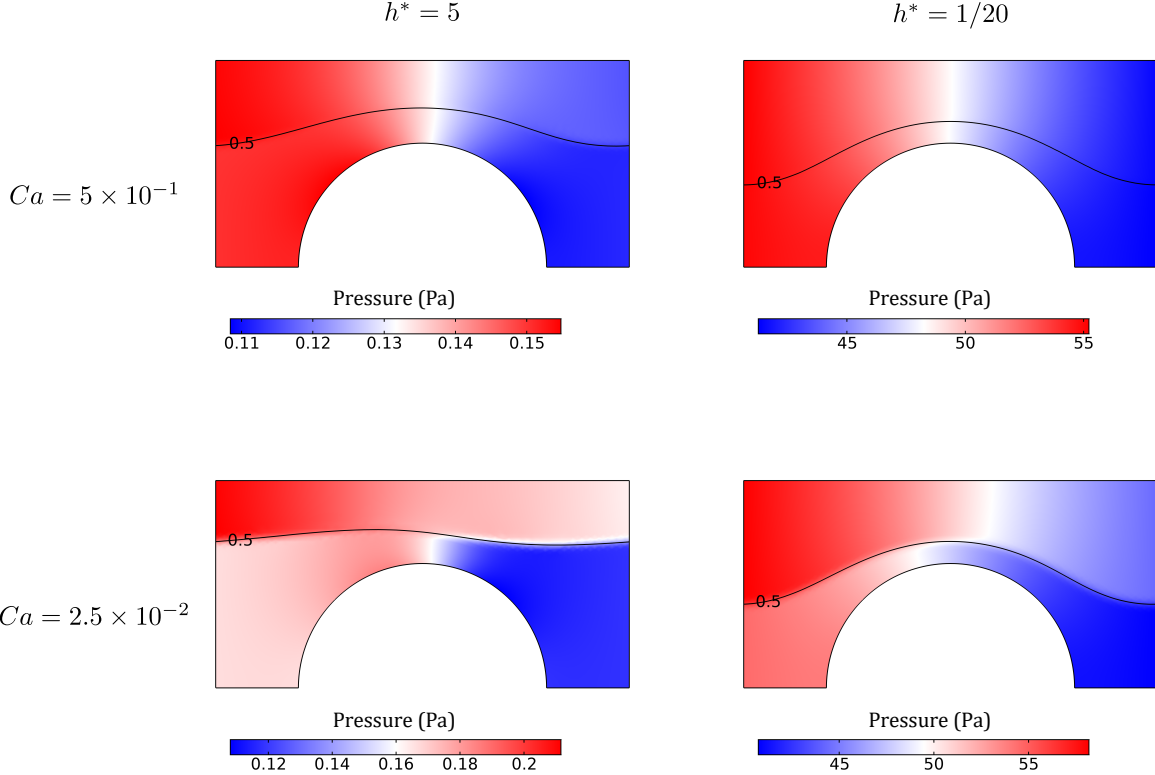


Figure 9 Comparison of the pressure field for two capillary numbers $Ca = 5 \times 10^{-1}$ (top row), $Ca = 2.5 \times 10^{-2}$ (bottom row) and two dimensionless gap thickness, with $h^* = 5$ (left column) and $h^* = 1/20$ (right column). The solid black line denotes the fluid-fluid interface given by the contour $\phi = 0.5$. Results obtained in UC4 at steady-state for $f_f = 0.25$ and $M = 1$.

terface where it forms a narrower constriction. In this case we also notice the appearance of recirculation cells in the wetting fluid. In the following we study the drag force terms and the effect of flow confinement, which is the key ingredient of this study.

C. Drag forces

We denote by d_{ij} the x -component of the drag force \mathbf{d}_{ij} exerted by phase i upon the phase j . We are interested here only by the x -component because it is the main flow direction, due to the inlet boundary conditions. Thus, we expect that $dp_i/dy \ll dp_i/dx$. We compute the fluid-fluid drag according to Eq. 9b. The viscous part is obtained through the velocity gradient available at the $\phi = 0.5$ -contour and the pressure part is obtained by application of the divergence theorem.

Fig. 11 shows all the drag force terms for each fluid as a function of the dimensionless gap

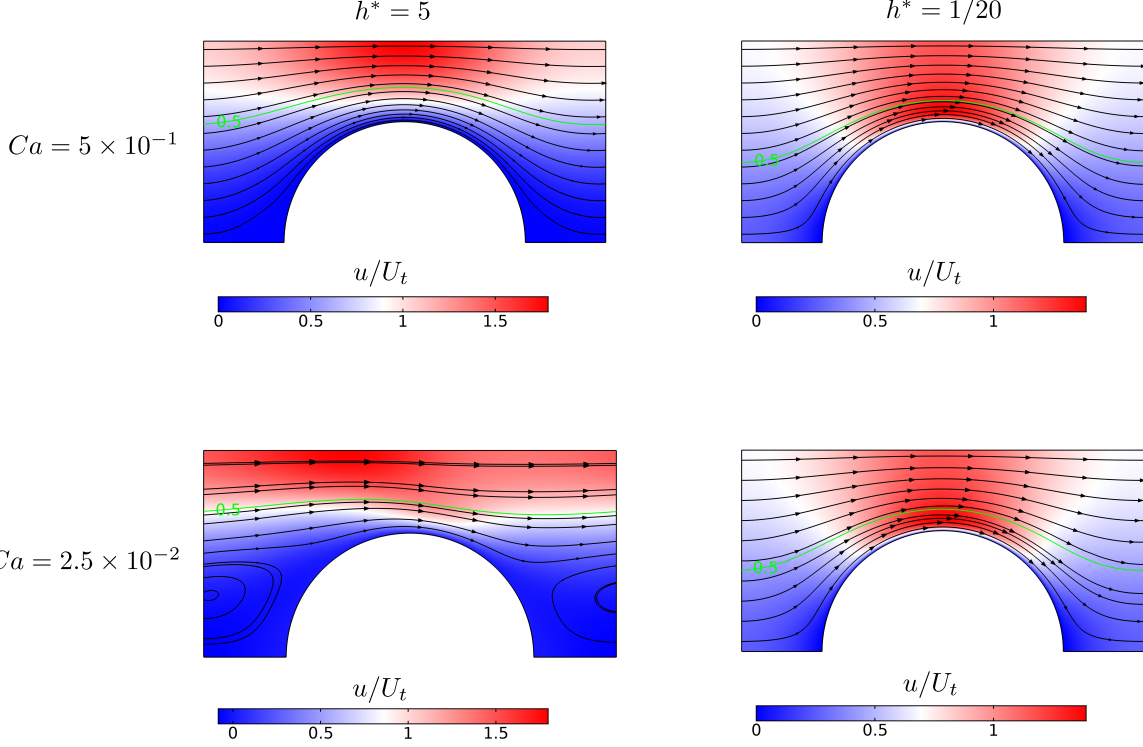


Figure 10 Comparison of the velocity field for two capillary numbers $Ca = 5 \times 10^{-1}$ (top row), $Ca = 2.5 \times 10^{-2}$ (bottom row) and two dimensionless gap thickness, with $h^* = 5$ (left column) and $h^* = 1/20$ (right column). The solid green line denotes the fluid-fluid interface given by the contour $\phi = 0.5$. Results obtained in UC4 at steady-state for $f_f = 0.25$ and $M = 1$.

and for different capillary numbers. The drag forces increase for a narrowing gap between the plates. That was to be expected since the inlet velocity and the outlet pressure are constant while we explore different values of gap thickness. Thus, the Darcean term in the Stokes-Darcy equations indicates that the pressure drop across the cell scales as h^{-2} .

The drag exerted upon the plates by the fluids also scales as h^{-2} , however according to Fig. 11, it would have been an error to anticipate that the pressure drop across the cell is entirely induced by the drag upon the plates for very thin gaps, i.e., very low permeability. Indeed, fluid-fluid and fluid-wedge drag also increases approximately as h^{-2} , thus we can already observe that the fluid-fluid drag never becomes negligible.

We now sum the drag terms of both fluids and we denote d_f the fluid-fluid drag exerted by the fluids upon each other and d_s the solid-fluid drag, which comprised only the plates in regard of fluid o and the plates along with the wedge in regard of the wetting fluid w . Fig. 12 shows the ratio of the fluid-fluid drag over the solid-fluid drag. Our results show that the fluid-

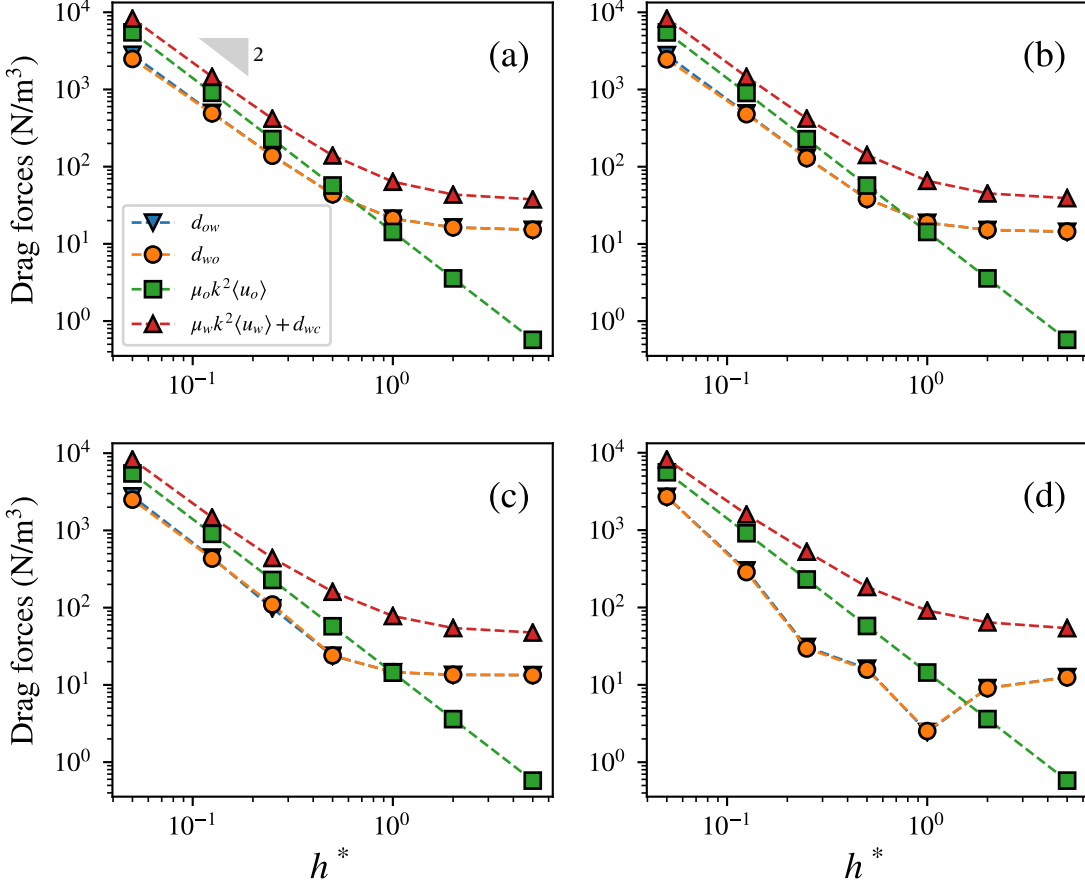


Figure 11 Comparison of each drag force term (x -component) as a function of the dimensionless gap between the plates for (a) $Ca = 5 \times 10^{-1}$, (b) $Ca = 1.25 \times 10^{-1}$, (c) $Ca = 2.5 \times 10^{-2}$ and (d) $Ca = 5 \times 10^{-3}$. The small discrepancy between the drag exerted by the fluids upon each other arises from the pressure jump across the interface (results in UC4 after steady-state was reached for $f_f = 0.25$ and $M = 1$).

fluid drag is not negligible and is more important for larger gap thickness and high capillary number. Indeed, it reaches 80% of the solid-solid drag value for $Ca = 0.5$ and $h^* = 5$. The ratio does not change between the largest gap investigated and the 2d-results. This indicates that the drag between the plates is already negligible for the widest gap $h^* = 5$. For a narrowing gap thickness the ratio d_f/d_s decreases for all capillary numbers. For $h^* < 1/2$, two configurations exist depending on the value of the capillary number. Either $Ca \geq 1.25 \times 10^{-1}$ and the ratio barely change with the gap or $Ca < 1.25 \times 10^{-1}$ and the ratio increases, i.e. the fluid-fluid drag increases compared to the solid-fluid drag, for a narrowing gap. In the following we discuss the two limit cases along with the transition stage between them.

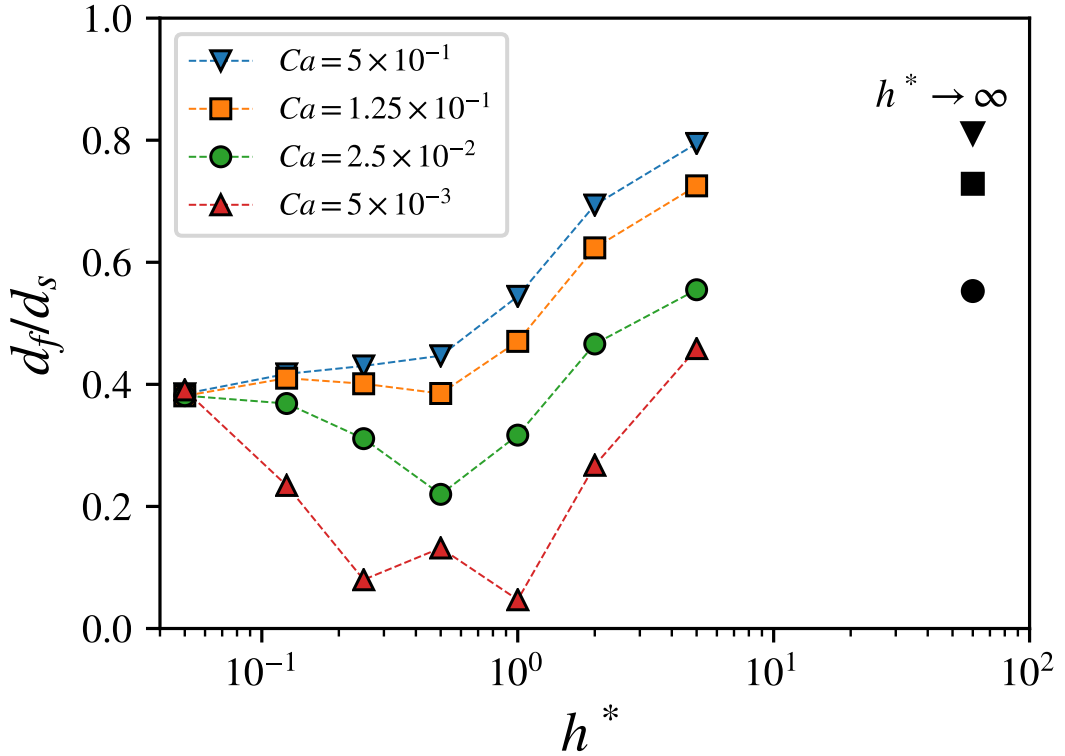


Figure 12 Ratios of fluid-fluid drag force over solid-fluid drag force as a function of the dimensionless gap between the plates and for different capillary numbers. Results for the pure 2d-simulations are given with solid black markers ($f_f = 0.25$ and $M = 1$).

1. First regime: thick gap regime

We now turn to the study of the first regime ($h^* \geq 1/2$) for which the fluid-fluid drag is decreasing compared to the solid-drag. For very wide gap the drag between the plates is insignificant and the only drag remaining are between the fluids and upon the wedge. As shown in Fig. 12 the gap thickness $h^* = 5$ is a very good approximation of the purely 2d-case in this regard. From there, the introduction of the perpendicular confinement drastically decreases the fluid-fluid drag value compared to the solid-drag value, especially for the non-wetting fluid which is initially in contact solely with the other fluid (Fig. 13).

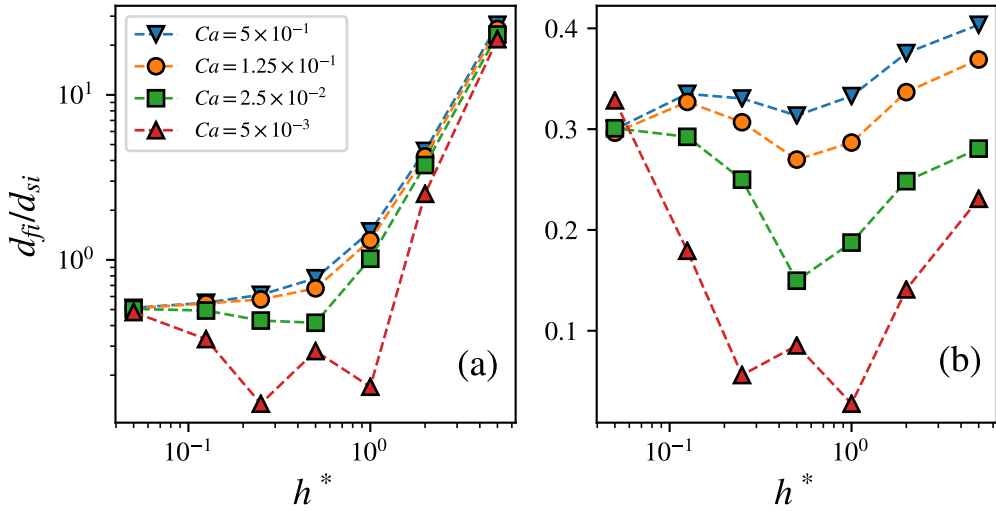


Figure 13 Comparison of the ratio given by the fluid-fluid drag over the solid-fluid drag for each fluid as a function of the dimensionless gap thickness. The results are given for different capillary numbers and for (a) the non-wetting fluid o and (b) the wetting fluid w ($f_f = 0.25$ and $M = 1$).

2. Second regime: thin gap regime

The thin gap regime ($h^* < 1/2$) is characterized by the predominance of the pressure contribution in the drag forces, which is related to the h^{-2} increasing of the pressure gradient induced by the Darcean terms. Here we denote the pressure part of the drag force d_{ij} as $d_{ij,p}$ ($d_{ij,p} = \frac{1}{S} \int_{\Gamma_{ij}} -p_i n_{ij}^x d\Gamma$) and the viscous part as $d_{ij,v}$ ($d_{ij,v} = \frac{1}{S} \int \mu_i (2\partial_x u n_{ij}^x + (\partial_y u + \partial_x v) n_{ij}^y)$). Fig. 14 compares the pressure and viscous part of the drag forces exerted upon fluid o by fluid w and the drag exerted by fluid w upon the wedge. For $h^* < 1/2$ the pressure part largely dominates over the viscous part. This last slightly increases for the viscous part of the drag upon the wedge whereas it decreases for the fluid-fluid drag.

V. CONCLUSION

In this study we conducted direct simulations of depth-averaged two-phases flows, and we investigated the effect of the permeability on the drag forces exerted upon the different phase interfaces. The permeability was changed by varying the Darcean term which arises from the depth-averaging, thus without altering the in-plane geometry. These drag terms have to be modelled to obtain the macroscopic momentum transport equations but the drag exerted

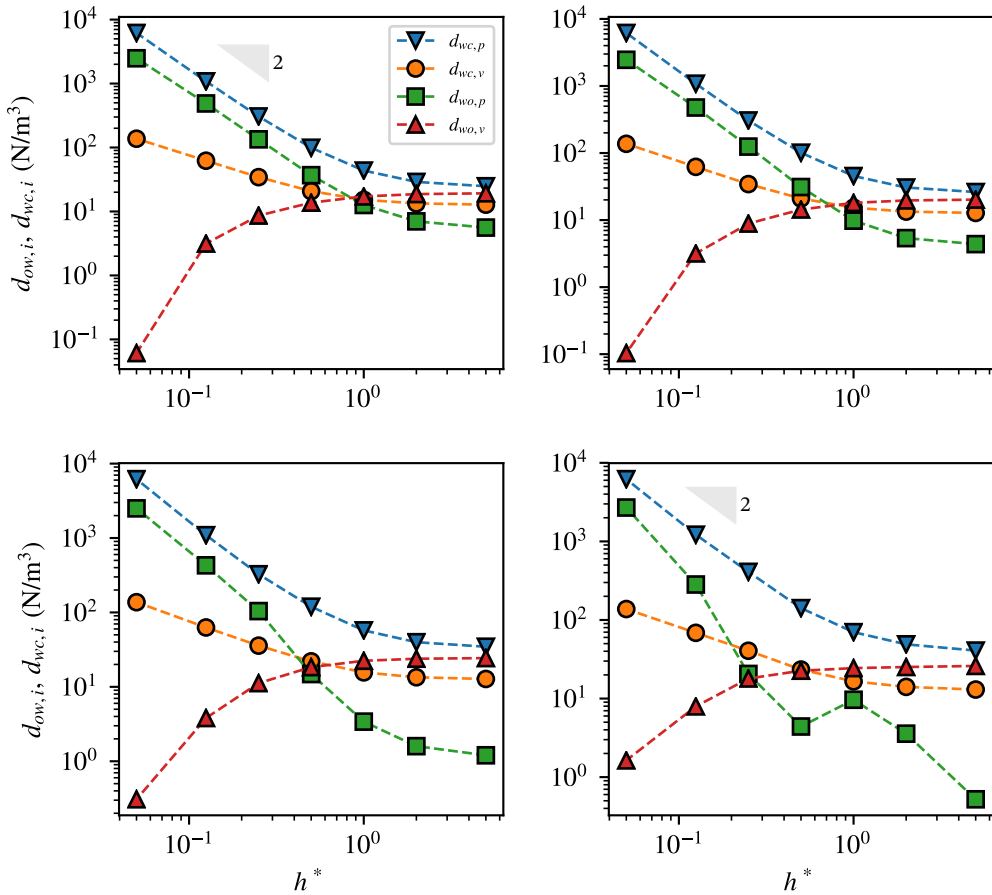


Figure 14 Comparison of the pressure and viscous part of the fluid-fluid drag d_{wo} and the fluid-wedge drag d_{wc} as a function of the dimensionless gap thickness and for different capillary numbers.

upon the the fluid-fluid interface is commonly neglected for flow driven by capillarity forces. Here we reproduced film-flow regime flow encountered in two-phases flows in high permeability porous media or in microfluidic devices. Even for a very thin gap between the plates, i.e. small permeability, the fluid-fluid tdrag force at the interface is not negligible. Two regimes are identified, (i) the thick gap regime is characterized by the decreasing fluid-fluid drag value compared to the solid-fluid drag. This is due to the introduction of the perpendicular confinement which scales as h^{-2} whereas the fluid-fluid drag, as well as the fluid-wedge drag, barely increase at this stage. (ii) The thin gap regime which depend on the capillary number.

REFERENCES

- Auriault, J., Sanchez-Palencia, E., 1986. Remarques sur la loi de darcy pour les écoulements biphasiques en milieu poreux. *Journal of Theoretical and Applied Mechanics*, Numéro Spécial , p141–156.
- Avraam, D.G., Payatakes, A.C., 1995. Generalized relative permeability coefficients during steady-state two-phase flow in porous media, and correlation with the flow mechanisms. *Transport in Porous Media* 20, 135–168. doi:doi:10.1007/bf00616928.
- Ayub, M., Bentsen, R.G., 1999. Interfacial viscous coupling: a myth or reality? *Journal of Petroleum Science and Engineering* 23, 13–26.
- Bacri, J.C., Chaouche, M., Salin, D., 1990. Modèle simple de perméabilités relatives croisées. *Comptes rendus de l'Académie des sciences. Série 2, Mécanique, Physique, Chimie, Sciences de l'univers, Sciences de la Terre* 311, 591–597.
- Bensimon, D., 1986. Stability of viscous fingering. *Physical Review A* 33, 1302.
- Bentsen, R.G., Manai, A.A., 1993. On the use of conventional cocurrent and countercurrent effective permeabilities to estimate the four generalized permeability coefficients which arise in coupled, two-phase flow. *Transport in Porous Media* 11, 243–262.
- Blunt, M.J., 2017. Multiphase flow in permeable media: A pore-scale perspective. Cambridge University Press.
- Bourbiaux, B.J., Kalaydjian, F.J., et al., 1990. Experimental study of cocurrent and countercurrent flows in natural porous media. *SPE Reservoir Engineering* 5, 361–368.
- Brooks, R., Corey, T., 1964. Hydraulic properties of porous media. *Hydrology Papers, Colorado State University* 24, 37.
- Clavier, R., Chikhi, N., Fichot, F., Quintard, M., 2017. Modeling of inertial multi-phase flows through high permeability porous media: Friction closure laws. *International Journal of Multiphase Flow* 91, 243–261.
- Cueto-Felgueroso, L., Juanes, R., 2014. A phase-field model of two-phase hele-shaw flow. *Journal of fluid mechanics* 758, 522.
- Davit, Y., Quintard, M., 2018. One-phase and two-phase flow in highly permeable porous media. *Heat Transfer Engineering* , 1–19.
- Dullien, F.A.L., 2012. Porous media: fluid transport and pore structure. Academic press.

- Dullien, F.A.L., Dong, M., 1996. Experimental determination of the flow transport coefficients in the coupled equations of two-phase flow in porous media. *Transport in Porous Media* 25, 97–120. doi:doi:10.1007/bf00141264.
- Ehrlich, R., 1993. Viscous coupling in two-phase flow in porous media and its effect on relative permeabilities@bookbear2013dynamics, title=Dynamics of fluids in porous media, author=Bear, Jacob, year=2013, publisher=Courier Corporation . *Transport in Porous Media* 11, 201–218.
- Fetter, C.W., Boving, T., Kreamer, D., 2017. Contaminant hydrogeology. Waveland Press.
- Guyon, E., Hulin, J.P., Petit, L., 1994. Hydrodynamique physique. interéditions.
- Heshmati, M., Piri, M., 2018. Interfacial boundary conditions and residual trapping: A pore-scale investigation of the effects of wetting phase flow rate and viscosity using micro-particle image velocimetry. *Fuel* 224, 560 – 578. URL: <http://www.sciencedirect.com/science/article/pii/S0016236118303971>, doi:doi:<https://doi.org/10.1016/j.fuel.2018.03.010>.
- Homsy, G.M., 1987. Viscous fingering in porous media. *Annual review of fluid mechanics* 19, 271–311.
- Jackson, S., Power, H., Giddings, D., Stevens, D., 2017. The stability of immiscible viscous fingering in hele-shaw cells with spatially varying permeability. *Computer Methods in Applied Mechanics and Engineering* 320, 606–632.
- Karadimitriou, N., Hassanzadeh, S., 2012. A review of micromodels and their use in two-phase flow studies. *Vadose Zone Journal* 11.
- Kopf-Sill, A.R., Homsy, G., 1988. Bubble motion in a hele–shaw cell. *The Physics of fluids* 31, 18–26.
- Lasseux, D., Quintard, M., Whitaker, S., 1996. Determination of permeability tensors for two-phase flow in homogeneous porous media: theory. *Transport in Porous Media* 24, 107–137.
- Lenormand, R., Touboul, E., Zarcone, C., 1988. Numerical models and experiments on immiscible displacements in porous media. *Journal of fluid mechanics* 189, 165–187.
- Li, H., Pan, C., Miller, C.T., 2005. Pore-scale investigation of viscous coupling effects for two-phase flow in porous media. *Physical Review E* 72. doi:doi:10.1103/physreve.72.026705.
- Liu, J., Ju, Y., Zhang, Y., Gong, W., 2019. preferential paths of air-water two-phase flow in porous structures with special consideration of channel thickness effects. *Scientific reports* 9, 1–13.
- Marle, C.M., 1982. On macroscopic equations governing multiphase flow with diffusion and chemical reactions in porous media. *International Journal of Engineering Science* 20, 643 – 662. doi:doi:[https://doi.org/10.1016/0020-7225\(82\)90118-5](https://doi.org/10.1016/0020-7225(82)90118-5).

- Maruvada, S., Park, C.W., 1996. Retarded motion of bubbles in hele–shaw cells. *Physics of fluids* 8, 3229–3233.
- Maxworthy, T., 1986. Bubble formation, motion and interaction in a hele-shaw cell. *Journal of Fluid Mechanics* 173, 95–114.
- Meiburg, E., Homsy, G., 1988. Nonlinear unstable viscous fingers in hele–shaw flows. ii. numerical simulation. *The Physics of fluids* 31, 429–439.
- Muskat, M., 1938. The flow of homogeneous fluids through porous media. *Soil Science* 46, 169.
- Nagel, M., Gallaire, F., 2015. Boundary elements method for microfluidic two-phase flows in shallow channels. *Computers & Fluids* 107, 272–284.
- Olsson, E., Kreiss, G., Zahedi, S., 2007. A conservative level set method for two phase flow ii. *Journal of Computational Physics* 225, 785 – 807. doi:doi:<https://doi.org/10.1016/j.jcp.2006.12.027>.
- Park, C.W., Homsy, G., 1984. Two-phase displacement in hele shaw cells: theory. *Journal of Fluid Mechanics* 139, 291–308.
- Rakotomalala, N., Salin, D., Yortsos, Y.C., 1995. Viscous coupling in a model porous medium geometry: Effect of fluid contact area. *Applied scientific research* 55, 155–169.
- Ramakrishnan, T.S., Goode, P.A., 2015. Measurement of off-diagonal transport coefficients in two-phase flow in porous media. *Journal of colloid and interface science* 449, 392–398.
- Roman, S., Soulaine, C., Kovscek., A.R., 2019. Pore-scale visualization and characterization of viscous dissipation in porous media. *Journal of Colloid and Interface Science* doi:doi:<https://doi.org/10.1016/j.jcis.2019.09.072>.
- Rose, W., 1988. Measuring transport coefficients necessary for the description of coupled two-phase flow of immiscible fluids in porous media. *Transport in Porous Media* 3, 163–171. URL: <https://doi.org/10.1007/BF00820343>, doi:doi:10.1007/BF00820343.
- Rothman, D.H., 1990. Macroscopic laws for immiscible two-phase flow in porous media: Results from numerical experiments. *Journal of Geophysical Research* 95, 8663. doi:doi:10.1029/jb095ib06p08663.
- Saffman, P.G., Taylor, G.I., 1958. The penetration of a fluid into a porous medium or hele-shaw cell containing a more viscous liquid. *Proceedings of the Royal Society of London. Series A. Mathematical and Physical Sciences* 245, 312–329.
- de Santos, J.M., Melli, T.R., Scriven, L.E., 1991. Mechanics of gas-liquid flow in packed-bed contactors. *Annual Review of Fluid Mechanics* 23, 233–260. doi:doi:10.1146/annurev.fl.23.010191.001313.

- Scott, P., Rose, W., et al., 1953. An explanation of the yuster effect. *Journal of Petroleum Technology* 5, 19–20.
- Stokes, J., Weitz, D., Gollub, J.P., Dougherty, A., Robbins, M., Chaikin, P., Lindsay, H., 1986. Interfacial stability of immiscible displacement in a porous medium. *Physical review letters* 57, 1718.
- Van Genuchten, M.T., 1980. A closed-form equation for predicting the hydraulic conductivity of unsaturated soils 1. *Soil science society of America journal* 44, 892–898.
- Whitaker, S., 1986. Flow in porous media II: The governing equations for immiscible, two-phase flow. *Transport in porous media* 1, 105–125.
- Whitaker, S., 2013. The method of volume averaging. volume 13. Springer Science & Business Media.
- Wyckoff, R.D., Botset, H.G., 1936. The flow of gas-liquid mixtures through unconsolidated sands. *Physics* 7, 325–345.
- Yiotis, A.G., Psihogios, J., Kainourgiakis, M.E., Papaioannou, A., Stubos, A.K., 2007. A lattice boltzmann study of viscous coupling effects in immiscible two-phase flow in porous media. *Colloids and Surfaces A: Physicochemical and Engineering Aspects* 300, 35 – 49. doi:doi: <https://doi.org/10.1016/j.colsurfa.2006.12.045>. proceedings of the Fourth International TRI/Princeton Workshop.
- Yuster, S., et al., 1951. Theoretical considerations of multiphase flow in idealized capillary systems, in: *Proceedings of the Third World Petroleum Congress*, E. Brill The Hague. pp. 437–445.
- Zarcone, C., Lenormand, R., 1994. Détermination expérimentale du couplage visqueux dans les écoulements diphasiques en milieu poreux. *Comptes rendus de l'Académie des sciences. Série II, Mécanique, physique, chimie, astronomie* 318, 1429–1435.
- Zhang, C., Oostrom, M., Wietsma, T.W., Grate, J.W., Warner, M.G., 2011. Influence of viscous and capillary forces on immiscible fluid displacement: Pore-scale experimental study in a water-wet micromodel demonstrating viscous and capillary fingering. *Energy & Fuels* 25, 3493–3505.

Appendix A: Approximation made on the drag force when considering a fluid-fluid flat interface

We conduct three-dimensional one-phase flow simulations into a microchannel to determine the approximation made on the drag calculation when considering that the fluid-fluid contour can be translated along the z -direction.

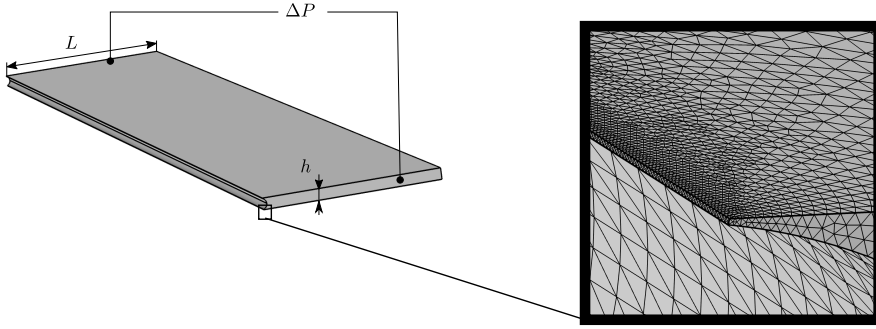


Figure 15 Microchannel with one side is a half-circle wall and the opposite side is a flat wall with $h/L = 1/16$ (left) and mesh detail at the small chamfer build after the cylinder extrusion (right).

One side of the microchannel is a half-circle wall to mimic a fluid-fluid interface whereas the opposite side is a flat wall (Fig. 15). We obtain the curved side by extruding a cylinder; thus a special treatment is done to correctly meshed the very thin part left, and we build very small chamfers (Fig. 15). We compute the drag force per unit surface area on each sidewall of the microchannel and plot in Fig. 16 the drag force exerted upon the curved side normalized with respect to the flat wall. The drag per unit surface area exerted upon the curved wall is roughly 70% of the drag per unit surface area upon the flat wall. Giving the greater extent of surface area for the curved wall, the difference regarding the drag value is negligible.

Appendix B: Comparison with a Boundary Element Method

Here we validate the Level Set (LS) code by comparison with a Boundary-Element Method (BEM) (Nagel and Gallaire, 2015), which relies on a surface discretization of the interface and a pseudo-analytical formulation in the bulk of the phases. This allows us to precisely locate the interface, even in the case of very thin film flow, and to carefully analyze the choice of parameters in Eq. 11.

The test case resembles the case study (Fig. 17). The model is initially fully saturated with fluid w , with the exception of the channel through which fluid o is injected. We test either the $\phi = 0.5$ contour is an appropriate definition for the fluid-fluid interface and in what extent the value of the initialization parameter ψ can change the interface position. In Fig. 18 we present the half-part of the model and the interface between the fluids at time $t = 2.5$, for an aspect

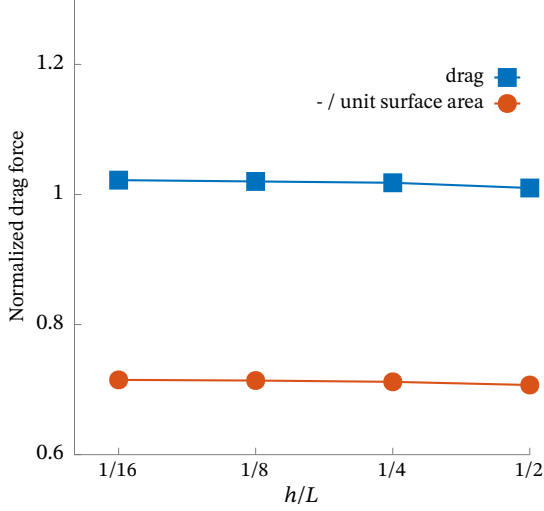


Figure 16 Drag force and drag force per unit surface area exerted upon the curved wall of the microchannel normalized with respect to the drag force exerted upon the flat wall. The drag exerted upon the curved solid wall is almost equal to the drag exerted upon the flat wall, since the smaller drag per unite surface area is almost fully compensated by the greater surface area. .

ratio h/L , where L is the width of the fluid o inlet channel. We present three different interfaces obtained with the LS method, depending on the initialization parameter value. This parameter is normalized with respect to the inlet velocity of fluid o , which is three times greater than the fluid w inlet velocity. The interface position obtained with the LS method is almost identical to that obtained with the BEM, regardless of value of ψ . However, the best results, especially regarding the interface tip position, is obtained for $\psi = U_o^{\text{inlet}}$.

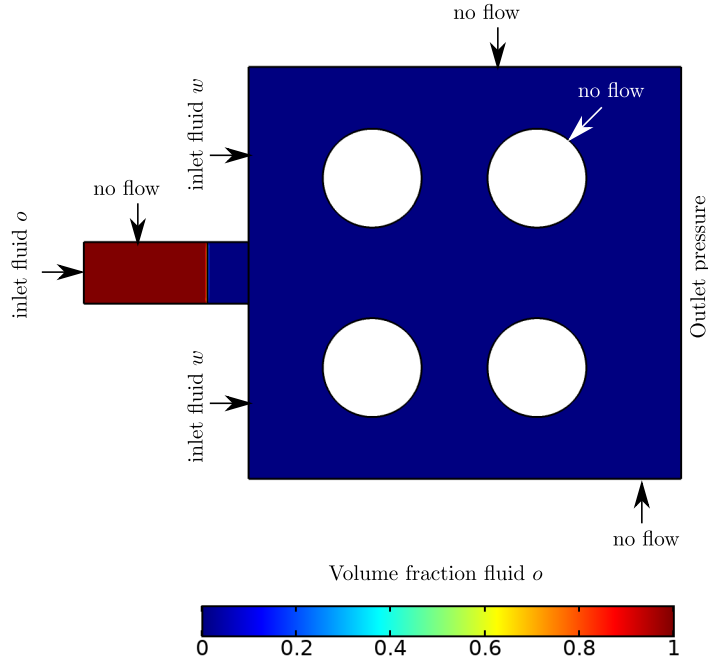


Figure 17 Test case for comparison between Level Set and Boundary Element methods. The flow is cocurrent from left to right and the viscosity is the same for both fluids.

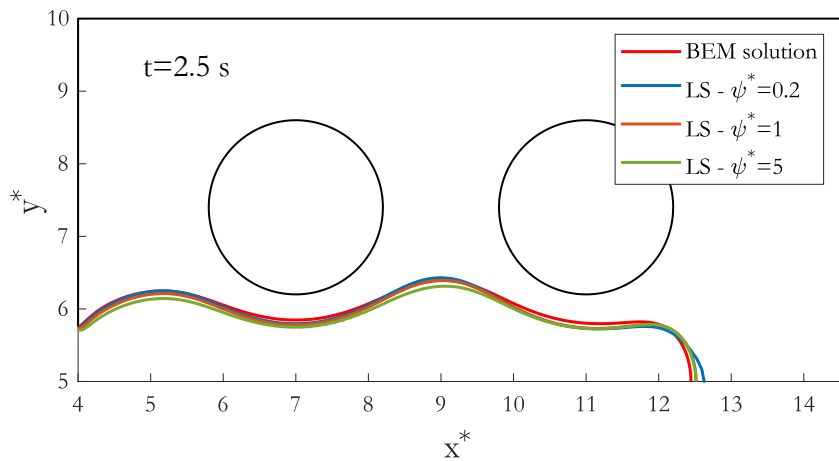


Figure 18 Interface position at time $t = 2.5$ s obtained for an aspect ratio $h/L = 0.25$ with a Boundary Element method and the Level Set method for different values of the dimensionless initialization parameter $\psi^* = \psi/U_o^{\text{inlet}}$.